1   Dear Editor,

2   Here there are the point by point replies of the comments of the reviewer 1 in red.

3   We hope that with this revision the paper can be considered acceptable for publication.

4   Prof. Mauro Guglielmin

5

6

7   The manuscript has been revised and I appreciate the answers/amendments the authors provide. However,
8   in my opinion, the concerns expressed the first previous review are only considered to a minimal extent,
9   still leaving some important questions.

10

11   The remaining points are:

12   - Line 83: the PACE borehole revealed some ice fills karst, but this is still not discussed further. Is it justified
13   to neglect this finding?

14   Yes, It is justified because the two small karst in reality were two fractures almost vertical crossed by the
15   first borehole for 1-2 meters filled by ice. More in general the examined area is avoided by the karst and
16   the fractures are generally not abundant. From some electrical resistivity soundings (not shown) carried out
17   in the area no traces of massive ice were found. To avoid possible confusion we change in the text and
18   instead of " small karst" we use the more appropriate term "fractures".

19   - In the figures, please state clearly what the different colors and line styles refer to.

20   DONE

21   - Figure 4,5 and Figure 8: the alpha value differs between the reconstructions using the synthetic and real
22   data, why? As seen in Figure 4 and 5, a variation can lead to significantly different results.

23   The regularization parameter alpha depends on the dataset and the noise level. Hence the three alpha
24   values used for the reconstructions with synthetic and real data are not related to each other.

25   - Fig. 9 is not cited in the manuscript text.

26   Sorry, there was an error because it was cited but with the wrong number (8 instead of 9). Now we correct
27   it but we expand more the sensitivity respect the thermal diffusivity as follows " The effects of the
28   different thermal diffusivities measured in the different facies of the SSB borehole are also illustrated in
29   Figure 8 where is possible to notice that the difference of temperature *a posteriori* between a model with a
30   constant diffusivity equal to the average value of the facies a between 0°C and -1°C (red dots) and the
31   model with the different diffusivities for each different facies layer (blue dots) is absolutely negligible (<
32   0.02°C) in all the depths with the exception of the uppermost (20 m) where the difference is higher but still
33   very low (0.06°C).

- The caption of Fig. 9 is not clear – where do the temperature ranges come from? As seen from Fig. 14 they probably represent the uncertainty in the temperature measurements.

Thanks for the comment. We rewrote the caption of Fig. 8 (ex 9) as follows: Fig. 8 Effects of different thermal diffusivity used in the model. The temperature profiles *a posteriori* of 2015 obtained in the case of a constant thermal diffusivity value of the more widespread facies (a) (red dots) and in the case of with a multilayers thermal diffusivities according the different facies according Fig. 6 (blue dots). The bars indicate the variations of the measured temperature in the same year.

Consequently, it would be interesting to investigate the effect of this temperature uncertainty on the reconstructed GST history, not only showing it along with the temperature anomalies resulting from the reconstructed GST history.

In order to investigate the effects of the accuracy of the measures and of their variations in the three examined years on the reconstructed GST history we added the variations of the reconstructed GST history using all the variation ranges of the measured temperature at all the depths in Fig. 10. It is visible that the pattern did not change and the different curves have a range of variations of a maximum of 0.3°C for the period between 1500 and 1970 while is less accurate for the cold period of the 80th.

- Please justify your answer to the comment to line 167: „Numerical methods for the estimation of the regularization parameter, like GCV and L-curve, are not always reliable and in our case they provide an underestimation of the best value."

Several mathematical papers in the literature (see e.g. [1-4] below) have proved that for every numerical method for the estimation of the regularization parameter exists at least an example where it fails.

[1] Hansen, P.C., Jensen, T.K., Rodriguez, G.: An adaptive pruning algorithm for the discrete L-curve criterion. J. Comput. Appl. Math. 198, 483–492 (2006)L. Reichel and G. Rodriguez.

[2] Old and new parameter choice rules for discrete ill-posed problems. Numer. Algorithms, 63(1):65-87, 2013.

[3] Hanke, M.: Limitations of the L-curve method in ill-posed problems. BIT 36, 287–301 (1996)

[4] Hansen, P.C.: Analysis of the discrete ill-posed problems by means of the L-curve. SIAM Rev. 34, 561–580 (1992)

In our application, we observe that GCV and L-curve do not provide a reliable estimation of the regularization parameter, in practice they provide an underestimation, because the reconstructed GST history has too large and non-physical oscillations.

- Lines 250 to 253: regarding the uncertainty in the reconstruction (which still needs to be determined in my opinion), is justified to give results in this precision (0.96 °C)?

Thanks for the comment. You are right. We modified the text as follows "Our reconstruction after the cold GST anomaly, between 1906 and 1941 AD, shows a slightly positive peak (ca. 0.1°C) in 1930 and afterwards a very unstable period with a first sharp decrease of temperature until 1989 (between -0.2 and -0.6°C) and a second even sharper increase, reaching in 2011 the uppermost GST anomaly value of the last 500 years (around 1°C).

71 Also the caption of the Fig. 10 is changed as follows: Figure 10. Comparison between the anomaly of the
72 mean annual GST reconstructed by SSB borehole (black thick line), its uncertainty range (red shaded) and
73 MAAT anomaly reconstructed for the European Alps by Christiansen and Ljungqvist (2011) (grey line with
74 dots; data available online at: ttps://www.ncdc.noaa.gov/paleo/study/12355) both respect the same
75 reference period (1880-1960).

76 - As mentioned the thermistor at the critical depth seemed to work properly, but this could have been
77 investigated by varying the data used in the inversion (sensitivity study, uncertainty ranges, see comment
78 above).

79 Thanks again, the uncertainty in the reconstruction due to the slight variations in the time (less than 0.1°C)
80 of the measured temperatures has been reported in the new Fig. 10 as a red shaded area and it is possible
81 to see that the uncertainty is similar to the accuracy of the thermistors between the 1500 and 1970 while is
82 less accurate for the cold period of the 80th.

83 - 2D model: what would be the influence of the vertical extension of the model (background gradient...)

84 The model concerns temperature anomalies, that is differences between the observed temperatures and
85 the background gradient. This latter is assumed linear (as normally used in boreholes of this depth, i.e.
86 Bodri and Chermak, 2007) and is substracted from the measured data before applying the inversion. In the
87 case of the "forward model" simulations (figure 14), we compute the solution of the PDE (1) and its 2d and
88 3d extensions, which represent models for the anomaly and thus do not deal directly with the background
89 gradient. Moreover To satisfy the criticism on the 2D models as requested by the reviewer we calculate the
90 temperature distribution considering the 3D effect as reported below.

91 - I still consider a 3D model necessary in order to assess the 3D-effect on the temperature distribution,
92 although the authors provide arguments that this would not yield further information.

93 Although we believe that considering the morphology of the site this effect was not relevant we calculate
94 the temperature distribution considering the 3D-effect of the mountain using a DEM with a resolution of 10
95 m (the best available for the area), considering the same thermal properties and heat flow used for the
96 reconstruction of the GST and we report the results of this new calculation together the 2D already showed
97 in the previous version of the manuscript in the new figure 14.

98 It is possible to observe that as expected the 3D-effect at least in this case study is negligible.

99 Moreover we change also the text of appendix 2 as follows" .....

100 First we computed the solution of the one-dimensional model (1). Next we computed the solution of the
101 corresponding three-dimensional model in a computational domain of 400X400 m centered around SBB
102 and 500 m deep, whose the top surface was obtained from a DEM (with a resolution of 10m). Such domain
103 was discretized with the GMSH program and the heat equation was solved using linear Lagrange finite
104 elements in space and backward Euler in time. The mesh was refined until numerical convergence was
105 observed and in Figure 14 we present the results for a mesh with 1.3 million of tetrehedra. The numerical
106 simulations were performed with the HPC cluster of the Dipartimento di Matematica of the Università di
107 Torino.

108 Figure 14 compares the temperature anomalies that each of the models would predict at SSB at present
109 time. The red dots are the predicted well anomalies at the depth of the thermometers at SSB. One can see

that the predictions of the two-dimensional model with flat terrain (blue line) almost coincide with those of the one-dimensional one. Furthermore, the two-dimensional model applied to the section with the steeper sides (the SSW-NNE one, orange line) gives rise to predictions that are within the instrumental error (±0.1°C) whereas the N-S section (red line), which has a flatter terrain, gives rise to predictions that are quite close to those of the one-dimensional model. The predictions of the 3D model (dashed black line) are very close to the 2D flat and the 2D N-S (with difference always < 0.03°C).

Finally, let us remark that for the forward model, a numerical 3D simulation takes hours to complete on 16 computing nodes of our HPC cluster. Using a numerical multi-dimensional simulator in the inverse problem would of course require to compute several times the forward model and would thus take a lot longer than the few seconds in which our proposed method can compute the reconstructed GST depicted in Fig. 10.

Minor:

- Please check again, if "°C" is used for absolute temperatures and "K" for temperature differences (and the gradient, Table 1), this makes the distinction easier. We used in all the text only °C degrees.

- Table 2: unit for thermal conductivity is not correct.

Thanks we correct it.

To summarize, the authors present interesting and valuable data which "deserves" a thorough investigation, which has not been done yet in my opinion. Therefore, I recommend another revision in order to do fully justice to the available data.

We hope that the reviewer can be satisfied by the sensitivity investigations regarding the effects of 3D, 2D models that clearly indicate that, at least, in this case the changes of temperature distribution with the morphological and topographical conditions are not relevant. This is possible here because respect other alpine mountain permafrost boreholes the location is less steep and asymmetrical and the summit area is much larger. Also the effects of the thermal diffusivity and of the alpha value were considered and in the first case is clear as the difference of thermal diffusivity related to the different facies of rocks and of their temperature are negligible too because the stratigraphy is very homogenous and the range of temperature is quite narrow and also because the porosity is very low.

Guglielmin Mauro[1]*, Donatelli Marco[2], Semplice Matteo[3], Serra Capizzano Stefano[2,4].

1* Department of Theoretical and Applied Sciences, Insubria University, Via Dunant 3, 21100 Varese mauro.guglielmin@uninsubria.it;

2 Department of Science and High Technology, Insubria University; 3 Department of Mathematics, University of Turin; 4 Department of Information Technology, Uppsala University.

GROUND SURFACE TEMPERATURE RECONSTRUCTION FOR THE LAST 500 YEARS OBTAINED FROM PERMAFROST TEMPERATURES OBSERVED IN THE STELVIO SHARE BOREHOLE, ITALIAN ALPS.

ABSTRACT

Here we present the results of the inversion of a multiannual temperature profile (2013, 2014, 2015) of the deepest borehole (235 m) in the mountain permafrost of the world located close to Stelvio Pass in the Central Italian Alps. The Stelvio Share Borehole (SSB) is monitored since 2010 with 13 thermistors placed at different depths between 20 and 235 m. The negligible porosity of the rock (dolostone, < 5%) allows to assume the latent heat effects also negligible. The inversion model here proposed is based on the Tikhonov regularization applied to a discretized heat equation, accompanied by a novel regularizing penalty operator. The general pattern of ground surface temperatures (GST) reconstructed from SSB for the last 500 years are similar to the mean annual air temperature (MAAT) reconstructions for the European Alps. The main difference with respect to MAAT reconstructions relates to post Little Ice Age (LIA) events. Between 1940 and 1989, SSB data indicate a cooling of 1°C. Subsequently, a rapid and abrupt GST warming (more than 0.8°C per decade) was recorded between 1990 and 2011. This warming is of the same magnitude as the increase of MAAT between 1990 and 2000 recorded in central Europe and roughly doubling the increase of MAAT in the Alps.

1 INTRODUCTION

The thermal regime of the uppermost ground is determined by the geothermal heat flow and by the fluctuations of temperature at the surface. If rock was homogeneous and no temperature change were to occur at the surface, the temperature would increase linearly with depth, unless spontaneous heat production is present on the vicinity of the well.. The gradient of this temperature increase would be governed solely by the magnitude of the terrestrial heat flow and by the thermal conductivity of the rock. However, variations of ground surface temperature (GST) propagate downwards into the rock as attenuating thermal waves, superimposed on the aforementioned linear temperature profile. The depth to which disturbances can be recorded is determined mainly by the amplitude and duration of the temperature change at the surface. Generally, propagation of climate signals is slow and it can take more than 1,000 years to reach the depth of 500m (Huang et al., 2000). For a better conservation of the climate signal in the thermal profile, no lateral heat advection (due for example to ground water flow) should be present (Lewis and Wang, 1992). Since normally no groundwater circulation is present within continuous permafrost in the polar areas but also in rocky areas within mountain permafrost, boreholes drilled in these areas are particularly suited for GST reconstructions.

Lachenbruch and Marshall (1986) were among the first to demonstrate that thermal profiles obtained from boreholes drilled in permafrost can be used to reconstruct ground surface temperature changes. These do not require calibration because the heat conduction equation is directly used to infer temperature changes at the ground surface. Today, the majority of permafrost boreholes used to reconstruct ground surface temperatures are located in the Polar regions of North America and Eurasia where the boreholes can be drilled on flat terrain, with negligible topographical effects, and with a

185 permafrost thicknesses typically exceed 100 m, thereby providing deep temperature logs and long ground
186 surface temperature reconstructions. On the other hand several factors like porosity, water/ice and latent
187 heat flows can influence significantly the thermal properties and the thermal signal especially measured in
188 frozen sediments boreholes as well discussed in Mottaghy and Rath (2006).

189 The Share Stelvio borehole (SSB) in the Italian Alps is the deepest drilled within permafrost in the mid-
190 latitude mountains of Europe. Because the permafrost thickness exceeds 200 m at this site it allows
191 reconstruction of GST for some centuries and much more than in the other mountain permafrost
192 boreholes.. In addition, the Stelvio borehole is located on a rounded summit with gentle side slopes.
193 Therefore, site-specific topographic influences are largely eliminated. As such, it is different to the other
194 boreholes drilled in permafrost in the Alps (e.g. PACE boreholes at Schilthorn or Stockhorn; see Harris et al.,
195 2003; Gruber et al.,2004; Hilbich et al., 2008; Harris et al., 2009).

196 Recent atmospheric warming (over the last century) in the European Alps has been roughly twice the global
197 average (Böhm et al., 2001; Auer et al., 2007). Despite its high sensitivity, no GST reconstruction based on
198 borehole thermal profiles is available for this part of the world. Instead, reconstructions of summer air
199 temperatures have been based on either tree-rings (e.g. Büntgen et al., 2006; Corona et al., 2010) or lake
200 sediments (e.g. Larocque-Tobler et al., 2010; Trachsel et al., 2010) for the last 500-1000 years, or both
201 (Trachsel et al., 2012). With rare exceptions (e.g. ice cores; Barbante et al., 2004), the other proxy data are
202 from sites at elevations that rarely exceed 2000m a.s.l. and all the other monitored permafrost boreholes in
203 Europe do not exceed 100 m of depth (see Harris et al., 2003). However, several papers describe GST
204 reconstructions for the last 500-1000 years using boreholes data at hemispheric or global scales (e.g.
205 Huang et al., 2000; Beltrami and Boulron, 2004).

206 The SSB data provides GST history from a high elevation site (3000 m a.s.l.). Such locations are important
207 because snow cover can affect significantly the GST (Zhang, 2005; Ling and Zhang, 2006; Cook et al., 2008).
208 They are also relevant with respect to glacier dynamics and their feedbacks with the global atmospheric
209 system (IPCC, 2013).

210 This paper reconstructs the ground surface temperatures inferred from this borehole and compares the
211 results with existing multiproxy reconstructions for the European Alps and elsewhere.

212

213 2 STUDY AREA

214 The Stelvio–Livrio area is a summer ski location, located between the Stelvio Pass (2758 m a.s.l.) and Mt
215 Livrio (3174 m a.s.l.), within the Stelvio National Park. The area is characterized by bedrock outcrops
216 (mainly dolostone), apart from some Holocene moraines (Figure 1a). The SSB borehole was drilled in 2009
217 and is only 10m from the PACE borehole, drilled in 1998 (46°30'59''N; 10°28'35''E, 3000 m a.s.l., Figure 1b).
218 Both boreholes are located on a flat barren summit surface oriented NNW-SSE. The side slopes (SSW and
219 NNE exposed) are gentle, the northern being only slightly steeper (14.1° vs 12.5° vs from the top down to
220 2900 m a.s.l.; Fig. 2, solid line). Despite their lithological homogeneity and their low porosity (< 5%, Berra,
221 personal communication), the two boreholes differ because in the PACE borehole two fractures filled by ice
222 were encountered at 42 and 90 m depth (Guglielmin et al., 2001) but no evidence of ice was observed
223 during the SSB drilling. Using PACE temperature profile and typical thermal conductivity and heat flow
224 values cited in literature (4.0 $Wm^{-1}K^{-1}$, Clauser and Huenges, 1995; 85 mWm^{-2}, Cermak et al., 1992),
225 permafrost thickness in the SSSB borehole was estimated to be around 220 m.

226

3 METHODS

3.1 Field data

The SSB borehole was drilled in early July, 2010, using refrigerated compressed-air-flush drilling technology. The stratigraphy was obtained by analyses of the cuttings (sampled every 10 m) and, for the first 100 m, through analysis of TV logging. Since September 2010, the thermal regime of the SSB borehole was monitored with thermometers placed according to the PACE protocol (Harris et al., 2001). The accuracy of the thermometers is 0.1°C and the resolution is 0.01°C. The thermistors recorded the daily ground temperature (minimum, maximum and average) at 20, 25, 35, 40, 60, 85,105,125,145,165,205,215 and 235 m of depth. Since 1998, the main climatic parameters at the site (air temperature, snow cover, incoming radiation) have been monitored. Below the 20m depth, no significant seasonal variations in temperature are recorded.

3.2 Laboratory data

The thermal properties of the three main facies observed in the stratigraphy were measured in the laboratory at three different temperatures (0°C, -1°C; -3°C). Thermal diffusivity and specific heatwere measured by NETZSCH Gerätebau GmbH (Selb, Germany) using a NETZSCH model 457 MicroFlashTM laser flash diffusivity apparatus. Thermal diffusivity measurements were conducted in a dynamic helium atmosphere at a flow rate of c. 100 ml/min between −3 °C and 0 °C. Specific heat capacity was measured using the ratio method of ASTM-E 1461 (ASTM, 2003) with an accuracy of more than 5%. Density of the rock at room temperature was determined using the buoyancy flotation method with an accuracy better than 5%. Thermal conductivity was calculated following Carlsaw and Jaeger (1959):

$$\lambda \lambda = \rho \rho * c_p * \kappa,$$

where λ is the thermal conductivity (W m^{-1} K^{-1}), $\rho \rho$ is the bulk density (gcm^{-3}), c_p is the specific heat capacity (Jg^{-1} K^{-1}), and κ is the thermal diffusivity (m^2 s^{-1}).

3.3 Theory

The temperature anomaly in the borehole at time t at depth z is modeled by the solution of the heat equation

$$\frac{\partial A}{\partial t} - \frac{\partial}{\partial z}\left(\kappa \frac{\partial A}{\partial z}\right) = 0 \quad (1)$$

for the domain $(t, z) \in (-t_{max}, 0) \times (0, z_{max})$. Note that equation (1) can be derived from the classical formulation of Carlsaw and Jaeger (1959) under the hypothesis that the density and the specific heat capacity are constant with respect to the depth z (see also Liu and Zhang, 2014), which is a good approximation for the SSB (see Section 4.1 and appendix). Further, we have indicated with t_{max} the earliest time for which we will reconstruct the GST and with z_{max} the depth of the borehole. Equation (1) can be solved to compute the temperature anomaly at any given past time t and depth z from the boundary values A(t; 0) which represent the GST history. If the GST data A(t,0) are piece-wise constant, the solution of the direct problem for equation (1) can be found explicitly (see Carlsaw and Jaeger, 1959). In our case, we need

to solve the inverse problem of finding the GST from the borehole data, which provide the anomaly measured at present (t=0) or past times (t>0) at some depth z in the borehole.

In order to exploit the abovementioned explicit solution, it is customary to approximate the GST with a piece-wise constant function (see Figure 3)

$$GST(t) = \begin{cases} \tau_k, & t \in [-t_k, -t_{k-1}] \\ \tau_\infty, & t \leftarrow t_N \end{cases} (2)$$

where t_k, for $k = 1,...,N$, is the sequence of times in the past where we want to compute the value of the GST, and the τ_k's are the unknown values to be computed. The diffusive nature of the heat equation has the effect that fine details of GST signals are averaged away as time progresses. Therefore, in the field data, one can find signals coming only from long wavelength GST variations occurred in the distant past, whereas short wavelength signals are observable only if produced in the more recent history. In order to take into account long and short wavelengths variations of GST where each of them makes sense, contrary to the common use of choosing uniformly spaced time points, we choose

$$t_k = (1 + 0.2k)^2$$

so that the reconstruction points are closer to each other in the recent past and more separated for distant ages. The choice of the parameter 0.2 is such that the reconstructed GST can contain signals of wavelength of at least 33 years from 1600 onwards, 23 years from 1800 onwards, 16 years from 1915 onwards, 9 years from 1985 onwards.

Once the sequence t_k is chosen, the relation between the borehole temperature at depth z_j predicted by the model and the unknown values τ_k of the GST anomaly is linear. When comparing the anomaly $A(z,t)$ described by the above equation with the measured data in the borehole, one has to take into account that measured data represent the superposition of the anomaly with a background signal (linearly increasing with depth) coming from the heat flow and past climatic changes since the Last Glacial Maximum as found for deeper boreholes by Safanda and Rajver (2001) or by Rath et al., (2012). This linear trend can be identified by linearly fitting the data from the deepest part of the borehole (below 60m in our case). Following (3), imposing that the borehole temperatures measured T_j years ago at depth z_j leads to a linear system

$$L\vec{\tau} = \vec{m}, (4)$$

where the column vector $\vec{\tau} = [\tau_1, \tau_2, ..., \tau_N, \tau_\infty]$ collects the unknown GST values, $\vec{m}$ is the column vector of detrended measured data and L is a matrix with M x (J + 1) entries (see the appendix). Each row in L (and entry in the vector m), corresponds to a measured temperature in the well at present or at some time in the past. In this fashion, the GST reconstruction can be based not only on a single temperature profile but also on the variation of the temperature profile between the present and some years ago. To the best of our knowledge, this possibility, which enhances the robustness of the reconstruction, has never been exploited before in the literature. Given the detrended measures $\vec{m}$, we must compute the vector $\vec{\tau}$ solving the linear system (4). However it is well known that the inverse problem for the heat equation (1) is severely ill-posed and thus solving directly the linear system (4) would lead to a computed GST that would be highly oscillating and very far from the true physical values for $\vec{\tau}$. It is then necessary to introduce a regularization process by modifying the original problem (4), in order to obtain an approximation that is well posed and less sensitive to errors in the right-hand-side of (4). Classical regularization techniques include the truncated singular value decomposition (TSVD) and the Tikhonov regularization in standard form (Hansen,

298 1998), applied in Beltrami and Boulron, (2004) and Liu and Zhang, (2014), respectively. In this paper, we
299 propose the use of the generalized Tikhonov regularization, where the damping term is measured by a
300 proper seminorm. In practice, instead of dealing with the linear system (4), we solve the minimization
301 problem

$$\min_{\vec{\tau}}\|L\vec{\tau} - \vec{m}\| + \alpha\|R\vec{\tau}\| \quad (5)$$

302 where $\alpha > 0$ is the regularization parameter and R is the regularization matrix. The use of a regularization
303 matrix R for this application is a novelty although several other regularization smoothing parameters were
304 already used (i.e. Shen et al., 1992; Rath and Mottaghy, 2007) If R is simply the identity matrix, then the
305 problem (5) reduces to the standard Tikhonov method used in Liu and Zhang, (2014). When α is large the
306 restored GST is very smooth but the differences between the measured data and the temperatures in the
307 well that would be computed by (4) from the recovered GST are large. On the contrary, when α is too small
308 the data fitting is good but the GST becomes highly oscillating due to the ill-posedness. A good tradeoff is
309 not trivial and several strategies can be explored for estimating an optimal value of α: as an example, the
310 generalized cross validation (Golub et al., 1979) often provides good results.

311 A common choice for R is a finite difference discretization of a differential operator (Hansen, 1998]. In this
312 paper, we consider a standard discretization of the Laplacian so that the constant and linear components of
313 the solution are not damped in the Tikhonov regularization, (5) while we have a penalization of high
314 oscillations. The details of the chosen regularization and of the GST inversion employed are described in the
315 appendix.

316 3.4 Validation on synthetic data

317 In order to validate our GST inversion method we have generated a synthetic data set as follows. An ideal
318 GST was chosen (dashed curve in Fig. 4) and equation (1) was solved by a finite difference method with a
319 spatial grid spacing of 1 m. Homogeneous Neumann boundary conditions were imposed at the well bottom
320 and the ideal GST as Dirichlet data at z=0, thus obtaining synthetic data for the measurements of
321 temperature in the well. The computed temperatures were saved for the depth at which the real
322 thermometers in SBB are located (see Section 3.1), for the present time, as well as for 1, 2 and 3 years
323 before present. We then used the generated data as input to the inversion algorithm described in the
324 previous section and compared the reconstructed GST with the ideal one used to generate the synthetic
325 data.

326 In the first experiment we fed our inversion algorithms only with the synthetic data for the present time.
327 The value of alpha that best fits the exact GST is alpha=0.15, but in Figure 4 one can see that also varying
328 this value by 33% the reconstructed GST does not vary significantly.

329 Next we fed the inversion algorithm also with the synthetic data for the past years. First, the inversion is
330 expected to be more accurate since the algorithm can average not only on the temperature at a given
331 depth but also on the variation of the temperature in the last years at that depth. Moreover, the algorithm
332 should also be more robust, since it relies on a larger data set. Both these effects can be appreciated in Fig.
333 5, where it can be seen that the inversion in the last 50 years is more accurate than the inversion of Fig. 4
334 and that a wider variation in the value of alpha is possible without affecting very much the quality of the
335 reconstruction.

336

4 RESULTS

4.1 Permafrost temperature, thermal properties and GST reconstruction

339 The SSB stratigraphy is characterized by four different facies of dolostone (Figure 6): a massive dolostone
340 (from grey to pinky grey) comprises more than 90% of the profile; three other facies (white dolostone,
341 black stratified limestone, brownish dolostone) are thin intercalations (maximum 3.5 meters of thickness
342 and located mainly in the first 42 m). In particular facies d, was not analysed for thermal analyses because is
343 very limited and it does not have any lateral continuity.

344 The mean annual thermal profiles of the last three years (2013-14-15) show a negative gradient between
345 20 m (a depth corresponding approximately to the depth of zero annual amplitude, ZAA) and 60 m that
346 does not vary (-0.8°C/100 m in all the three years). At greater depth, the gradient is positive with slightly
347 different slopes between 60-105; 105-125; 125-205; 205-215 and 215-235 (Figure 7 and Table 1).

348 Table 2 shows the thermal properties of the three main stratigraphic facies encountered in the borehole.
349 Facies a and c show similar density and thermal properties while facies b has higher density and higher
350 conductivity. All facies have heat capacity values that increase with a decrease of temperature. In facies a,
351 this behavior occurs also for thermal conductivity and diffusivity values. In contrast, facies b and c show a
352 reversed bell shape behavior, with the minimum value recorded at -1°C and an absolute maximum at -3°C.
353 Therefore, from a thermal point of view, only facies b is different. Moreover, at depths below the level of
354 zero annual amplitude, this facies occurs only at depths of 34.5m and 90 m with a negligible thickness (2
355 and 1 m respectively) and at 142.5 m and 205 m where it reaches 3-3.5 m in thickness. Clearly, the thermal
356 influence of this facies is negligible, indeed, the gradient between 60 and 235 m is approximately the same
357 as that   between 60 and 105 m and between 125 and 205 m. The effects of the different thermal
358 diffusivities measured in the different facies of the SSB borehole are also illustrated in Figure 8 where is
359 possible to notice that the difference of temperature *a posteriori* between a model with a constant
360 diffusivity equal to the average value of the facies a between 0°C and -1°C (red dots) and the model with
361 the different diffusivities for each different facies layer (blue dots) is absolutely negligible (< 0.02°C) in all
362 the depths with the exception of the uppermost (20 m) where the difference is higher but still very low
363 (0.06°C).

364 According to the model proposed in the Methods, we found the best fitting with the thermal profiles
365 (Figure 7) using an heat flow of 70 mWm^{-2} (Della Vedova et al., 1995), a thermal diffusivity value equal to
366 the mean between the value obtained for 0°C and -1°C for facies a, which is the more widespread in the
367 borehole and an alpha value of 0.95 as shown in figure 9.

368 The linear system (4) was assembled including the detrended data measured at SSB in 2015 ($T_j = 0$, in
369 2014 ($T_j = 1$ and 2013 ($T_j = 2$, at the 13 depths listed in Section 3.1, resulting in 39 equations. The
370 anomalies of the GST reconstruction obtained with respect to the reference period between 1880 and 1960
371 has been computed using the value of $\alpha = 0.95$ for the regularization parameter (Figure 10).

372

5 DISCUSSION

5.2.1 GST and current air temperatures

375 In cryotic environments, snow cover can influence GST variability both in space and in time (e.g. Zhang,
376 2005; Schmidt et al., 2009; Morse et al., 2012; Rodder and Kneisel, 2012; Schmid et al., 2012; Guglielmin et
377 al., 2014). This is especially the case for alpine areas where topography influences both the re-distribution
378 of the snow by wind-drift and actual snow cover evolution (e.g. melting date and duration**).** Nevertheless,
379 GST and air temperature are well correlated (R^2 = 0.8027) and present a very similar pattern over the last
380 15 years with only a slight warming (Figure 11). This relatively slight effect of snow at this site is probably
381 due to the high wind velocities during winter that, on average, prevent buildup of a thick snowpack. Figure
382 12 illustrates the temporal variability of snow cover on the GST. In general, the highest (>±5°C) differences
383 between mean daily GST and mean daily air temperature occur when there are large drops of air
384 temperature during the winter. Sometimes, large differences occur also when there are large drops of air
385 temperature during the summer where there is little or no snow cover, because of high solar radiation that
386 heats the ground surface. Correlation is even better between monthly mean air temperature, mean annual
387 air temperature (MAAT) and mean annual ground surface temperature (MAGST) (R^2 = 0.8712 for this
388 latter). This agrees with the results of Zhang and Stamnes, (1998) who found that, in a flat area in northern
389 Alaska, changes in seasonal snow cover had a smaller effect than MAAT on the ground thermal regime.

5.2.2. GST Fluctuations between 1950 and today

391 Our reconstruction after the cold GST anomaly, between 1906 and 1941 AD, shows a slightly positive peak
392 (ca. 0.1°C) in 1930 and afterwards a very unstable period with a first sharp decrease of temperature until
393 1989 (between -0.2 and -0.6°C) and a second even sharper increase, reaching in 2011 the uppermost GST
394 anomaly value of the last 500 years (around 1°C).

395 On a regional scale, the Stelvio data can be compared with the MAAT obtained for the Alps by Christiansen
396 and Ljungqvist, (2011) (Figure 10) and Trachsel et al., (2010). The maximum of the slight temperature
397 increase during the first half of the XX century in the Stelvio data (1930) falls exactly in the middle of the
398 relative warming period between 1925 and 1935 in the Alps found by Trachsel et al., (2010) and is in good
399 agreement with the date (1928) indicated by Christiansen and Ljungqvist, (2011). Later, the sharp GST
400 anomaly decrease was delayed in the Stelvio data (1989) with respect to 1950-1965 period found by
401 Trachsel et al., (2010) and 1965-1975 period found by Christiansen and Ljungqvist, (2011). Finally, the most
402 recent increase of temperature culminated in the Alps in 1994 (Christiansen and Ljungqvist, 2011) while in
403 the Stelvio data at 2011.

5.2.3 The Little Ice Age (LIA)

405 The Stelvio reconstruction shows a long period of negative anomaly between 1560 and 1860 AD with the
406 colder conditions (< -2*S.D.) between 1683 and 1784 AD with a peak of -1.5°C around 1730 AD. This period
407 of negative anomaly falls within this well-known cooling period (LIA). It is recognized in several kinds of
408 proxy data although there are differences both in magnitude and in timing across the world. According to
409 Neukom et al., (2014), synchronous cold temperature anomalies occurred at decadal scale in both
410 hemispheres between 1594 and 1677 AD. They also found two phases of extreme cold temperature in the
411 Northern Hemisphere with the first between 1570 and 1720 AD and the second between 1810 and 1855.
412 Syntheses of the LIA in the European Alps have been presented by Trachsel et al., (2012) and Christiansen
413 and Ljungqvist, (2011). Considering the common colder periods in these two Alpine syntheses, the LIA has
414 three main negative peaks at 1570-1600; 1685-1700 and 1790-1820 AD.

415 The LIA period has been also characterized by a widespread worldwide glacier advance, although the
416 comparison between glacial evidences and temperature fluctuations are problematic because glaciers

417 respond with different time scales (mainly depending on their size) and reflect also the precipitation
418 regime, which is even more variable in space and time. According to Holzhauser et al., (2005), the LIA
419 advance of the main Swiss Glaciers has three peaks around respectively 1350, 1640 and 1820-50 AD with
420 the two later phases almost synchronous also in the Eastern Alps (Nicolussi and Patzelt, 2000).

421 Close to the location of the Stelvio borehole, the maximum LIA advance was diachronous. Nearby glaciers
422 show a maximum LIA advance in 1580 AD (Trafoi Valley glacier; Cardassi, 1995), around 1770 AD (Solda
423 Glacier; Arzuffi and Pelfini, 2001) and in 1600 AD (La Mare Glacier; Carturan et al., 2014).

424 The borehole area was presumably overcapped by the Vedretta Piana Glacier until 1868. Due to the
425 geomorphological position (on a watershed divide) the possible glacier should have been very thin and
426 possibly cold based, as already stressed by Guglielmin et al., (2001). On the other hand, considering figure
427 10, the glacier should have been present in the borehole area with a buffering effect only between 1711
428 and 1834 AD, with a peak at 1760, when the difference between the GST anomaly and the MAAT anomaly
429 was maximum. This peak is pretty similar to the peak of the LIA in the Solda Glacier (1770 AD) but not to
430 the peak in the Trafoi glacier (1580 AD); this could be related to Vedretta Piana having a more similar
431 glacier size and aspect (NE-N) to the Solda Glacier than to the Trafoi Glacier, although this latter is the
432 closest to the Vedretta Piana.

433 **5.2.4 Other permafrost borehole temperature reconstructions**

434 Several deep Alaskan boreholes have been used to demonstrate the XX century warming (e.g. Lachenbruch
435 and Marshall, 1986; Lachenbruch et al., 1988) but only a few studies in Europe illustrate GST
436 reconstructions that span a time period greater than 100-150 years (e,g, Isaksen et al., 2001, Guglielmin,
437 2004). In North America, only Chouinard et al., (2013) shows GST pattern of the last 300 years in the
438 context of the permafrost of Northern Quebec. There, after the LIA (1500-1800 AD), it was found an almost
439 constant and marked warming of ca 1.4 °C until 1940, followed by a cooling episode (≈0.4 °C) which lasted
440 40–50 yr, and finally a sharp ≈1.7 °C warming over the past 15 yr.

441 There is a some similarity between the Stelvio reconstruction and the pattern of Canadian permafrost GST
442 reported by Chouinard et al., (2013) after the LIA. Indeed, also in our site there was an almost simultaneous
443 but greater cooling (0.9°C) in the period between 1941 and 1989, followed by a sharp warming of ca 1.7°C.
444 On the other hand, GST reconstructions can be obtained with different models and it is interesting to
445 compare our data with, for example, the PMIP3/CMIP5 simulations that include the effect of aerosol
446 forcing by Garcia-Garcia et al., (2016): there, in the last 500 years, the GST shows a cold anomaly (LIA)
447 between 1582 and 1840, with the most negative peaks between 1798 and 1840, slightly delayed with
448 respect to our data.

449

450 # 5 CONCLUSIONS

451 The general climatic pattern of the last 500 years recorded by this mountain permafrost borehole is similar
452 to the majority of other studies in the European Alps and Central Europe. The main difference concerns
453 post LIA events. In fact, the different multidisciplinary proxies considered (see Figure 13) do not indicate
454 cooling between 1940 and 1989, with the exceptions of the shorter and less severe cooling found for the
455 Alps. It is also relevant to stress that the rapid and abrupt GST warming (more than 0.8°C per decade)
456 recorded between 1990 and 2011 in the Stelvio borehole data is similar to the warming recorded in

457 permafrost in northern Quebec. This warming trend is of the same magnitude as the increase of MAAT
458 between 1990 and 2000 in Central Europe (Dobrovlny et al., (2010), and is approximately double that found
459 for the MAAT in the Alps and for Europe as a the whole (Luterbacher et al., 2004).

460 The Stelvio borehole ground surface temperature reconstruction also allows one to estimate changes in the
461 Vedretta Piana glacier. This glacier presumably buried the site of the Stelvio borehole with an ice thickness
462 sufficient to exert a significant buffering effect upon the ground thermal regime between 1711 and 1834
463 AD. This was a time when the difference between the Stelvio GST anomaly and the MAAT anomaly was
464 greatest.

465

466 6 REFERENCES

467 Arzuffi, L. and Pelfini, M., I testimoni dei cambiamenti climatici, Neve e Valanghe, 43, 44–53, 2001.

468 Auer, I., Böhm, R., Jurkovic, A., Lipa, W., Orlik, A., Potzmann, R., Schöner, W., Ungersböck, M., Matulla, C.,
469 Briffa, K., Jones, P., Efthymiadis, D., Brunetti, M., Nanni, T., Maugeri, M., Mercalli, L., Mestre, O., Moisselin,
470 J.M., Begert, M., Müller-Westmeier, G., Kveton, V., Bochnicek, O., Stastny, P., Lapin, M., Szalai, S.,
471 Szentimrey, T., Cegnar, T., Dolinar, M., Gajic-Capka, M., Zaninovic, K., Majstoroviv, Z and Nieplova, E.
472 HISTALP-historical instrumental climatological surface time series of the Greater Alpine Region, Int. J.
473 Climatol., 27, 17–46, 2007.

474 Barbante, C., et al. Historical record of European emissions of trace elements to the atmosphere since the
475 1650s from alpine snow/ice cores drilled near Monte Rosa, Environ. Sci. Technol. 38,15, 4085–4090, 2004.

476 Beltrami, H. and Bourlon, E. Ground warming patterns in the northern hemisphere during the last five
477 centuries, Earth Planet. Sc. Lett., 227, 169–177, 2004.

478 Bodri, L. and Cermak, V., Climate changes of the last millennium inferred from borehole temperatures:
479 results from the Czech Republic Part I, Global and Planetary Change, 98, 111-125,1995.

480 Böhm, R., Auer, I., Brunetti, M., Maugeri, M., Nanni, T.and Schöner W. Regional temperature variability in
481 the European Alps: 1760-1998 from homogenized instrumental time series, Int. J. Climatol., 21, 1779–1801,
482 2001.

483 Büntgen, U., Frank, D. C., Nievergelt, D. and Esper, J., Summer temperature variations in the European Alps,
484 A.D. 755–2004, J. Climate, 19, 5606–5623.,2006.

485 Cardassi, S.P. Geologia del Quaternario e geomorfologia della Valle di Trafoi. Master's Thesis, University of
486 Milan, 1995.

487 Carlsaw, H.S. and Jaeger, J.C. Conduction of Heat in Solids. Oxford Univ. Press, New York. 510 pp. 1959.

488 Carturan, L., Baroni, C., Carton, A., Cazorzi, F., Dalla Fontana, G., Delpero, C., Salvatore, M.C., Seppi, R. and
489 Zanoner, T., Reconstructing fluctuations of La Mare Glacier (Eastern Italian Alps) in the Late Holocene: new
490 evidence for a Little Ice Age maximum around 1600 ad., Geografiska Annaler: Series A, Physical Geography,
491 96, 287–306, 2014.

Cermak, V., Balling, N., Della Vedova, B., Lucazeau, F., Pasquale, V., Pellis, G., Schulz, R. and Verdoya, M., Heat-flow data (Italy). In: Blundell, D., Freeman, R., Mueller, St. (Eds.), A Continent Revealed: The European Geotraverse Database. Cambridge Univ. Press, Cambridge, pp. 49– 57, 1992.

Chouinard, C., Fortier, R. and Mareschal J.C. Recent climate variations in the subarctic inferred from three borehole temperature profiles in northern Quebec, Canada, Earth and Planetary Science Letters, 263, 355– 369, 2007.

Christiansen, B. and Ljungqvist, F. C. Reconstruction of the extratropical NH mean temperature over the last millennium with a method that preserves low-frequency variability, J. Climate, 24, 6013-6034, 2011.

Clauser C, and Huenges E. Thermal conductivity of rocks and minerals. In Rock Physics and Phase Relations. A Handbook of Physical Constants, Ahrens TJ (ed). AGU Reference Shelf 3. American Geophysical Union: Washington; 105–126, 1995.

Cook, B.I., Bonan, G.B., Levis, S. and Epstein, H.E., The thermoinsulation effect of snow cover within a climate model, Clim. Dyn, 31, 107–124, 2008.

Corona, C., Guiot, J., Edouard, J.L., Chalié, F., Büntgen, U., Nola, P. and Urbinati, C., Millennium-long summer temperature variations in the European Alps as reconstructed from tree rings. Climate of the Past, 6, 379-400, 2010.

Della Vedova, B., Lucazeau, F., Pasquale, V., Pellis, G. and Verdoya., M. Heat flow in the tectonic provinces crossed by the southern segment of the European Geotraverse, Tectonophysics, 244 ,57-74, 1995

Dobrovolný, P., Moberg, A., Brázdil, R., Pfister, C., Glaser, R., Wilson, R., van Engelen, A., Limanówka, D., Kiss, A., Halíˇcková, M. Macková, J. Riemann, D. Luterbacher, J. and Böhm R., Monthly, seasonal and annual temperature reconstructions for Central Europe derived from documentary evidence and instrumental records since AD 1500, Climatic Change, 101, 69–107, 2010.

García-García, A., Cuesta-Valero, F. J., Beltrami, H. and Smerdon, J. E. Simulation of air and ground temperatures in PMIP3/CMIP5 last millennium simulations: implications for climate reconstructions from borehole temperature profiles, Environmental Research Letters, 11, 044022, 2016

Golub, G. H., Heath M. and Wahba G., Generalized Cross-Validation as a Method for Choosing a Good Ridge Parameter, Technometrics, 21 ,2, 215-223, 1979.

Gruber, S., King, L., Kohl, T., Herz, T., Haeberli, W. and Hoelzle, M., Interpretation of geothermal profiles perturbed by topography: the Alpine permafrost boreholes at Stockhorn Plateau, Switzerland, Permafrost and Periglacial Processes, 15, 349–357, 2004.

Guglielmin, M., Observations on permafrost ground thermal regimes from Antarctica and the Italian Alps, and their relevance to global climate change, Global and Planetary Change, 40, 159–167, 2004.

Guglielmin, M., Cannone, N. and Dramis, F., Permafrost-glacial evolution during the Holocene in the Italian Central Alps, Permafrost Periglacial Processes, 12, 111–124, 2001

Guglielmin, M., Worland, M.R., Baio, F. and Convey, P., Permafrost and snow monitoring at Rothera Point (Adelaide Island, Maritime Antarctica): Implications for rock weathering in cryotic conditions, Geomorphology, 225, 47–56, 2014.

Hansen, P., Rank-Deficient and Discrete Ill-Posed Problems, Society for Industrial and Applied Mathematics, 1998.

Harris, C., Haeberli, W., Vonder Muhll, D. and King, L., Permafrost monitoring in the high mountains of Europe: the PACE Project in its global context, Permafrost and Periglacial Processes, 12, 3 – 11, 2001.

Harris, C., Vonder Mühll, D, Isaksen, K., Haeberli, W., Sollid, J.l., King, L., Holmlund, P., Dramis, F., Guglielmin, M. and Palacios, D., Warming permafrost in European mountains, Global and Planetary Change, 39, 215-225, 2003.

Hilbich, C., Hauck, C., Hoelzle, M., Scherler, M., Schudel, L., Völksch, I., Vonder Mühll, D. and Mäusbacher, R., Monitoring mountain permafrost evolution using electrical resistivity tomography: a 7-year study of seasonal, annual, and long-term variations at Schilthorn, Swiss Alps, J. Geophys. Res., 113, F01S90. 2008.

Holzhauser, H., Magny, M. and Zumbühl, H.J., Glacier and lake-level variations in west-central Europe over the last 3500 years, The Holocene, 15, 6, 789–801, 2005.

Huang, S., Pollack, H. N. and Shen, P. Y., Temperature trends over the last five centuries reconstructed from borehole temperatures, Nature, 403, 756–758, 2000.

IPCC. Summary for policymakers, In Climate Change 2013: The Physical Science Basis. Contribution of Working Group I to the Fifth Assessment Report of the Intergovernmental Panel on Climate Change, Stocker, T.F., Qin, D., Plattner, G.K., Tignor, M.S.K., Allen, J., Boschung, A., Nauels, Y., Xia, Y., Bex, V., Midgley, P.M., (eds). Cambridge University Press: Cambridge, UK and New York, NY, 2013.

Isaksen, K., Vonder Muhll, D., Gubler, H., Kohl, T. and Sollid, J.L., Ground surface-temperature reconstruction based on data from a deep borehole in permafrost at Janssonhaugen, Svalbard, Annals of Glaciology, 31, 287– 294. 2001.

Lachenbruch, A.H. and Marshall, B.V., Changing climate: geothermal evidence from permafrost in the Alaskan Arctic, Science 234, 689– 696, 1986.

Lachenbruch, A.H., Cladouhos, T.T. and Saltus, R.W., Permafrost temperature and the changing climate. "Permafrost", 5th International Permafrost Conference Proceedings, vol. 3. Tapir Publishers, Trondheim, Norway, pp. 9–17, 1988.

Larocque-Tobler, I., Grosjean, M., Heiri, O., Trachsel, M., and Kamenik, C. Thousand years of climate change reconstructed from chironomid subfossils preserved in varved lake Silvaplana, Engadine, Switzerland, Quaternary Science Rewiews, 29, 1940–1949, 2010.

Lewis, T. J. and K. Wang, Influence of terrain on bedrock temperatures, Palaeogeogr. Palaeoclimatol. Palaeoecol. 98, 87–100, 1992

Ling, F. and Zhang, T.J., Sensitivity of ground thermal regime and surface energy fluxes to tundra snow density in northern Alaska, Cold Reg. Sci. Technol., 44, 121–130, 2006.

Liu J. and Zhang T., Fundamental solution method for reconstructing past climate change from borehole temperature gradients, Cold Regions Science and Technology, 102, 32-40, 2014.

Luterbacher, J., Dietrich, D., Xoplaki, E., Grosjean, M., and Wanner, H., European seasonal and annual temperature variability, trends, and extremes since 1500, Science, 303, 1499–1503,2004.

566 Morse, P.D., Burn, C.R. and Kokelj, S.V., Influence of snow on near-surface ground temperatures in upland
567 and alluvial environments of the outer Mackenzie Delta, N.W.T. Can. J. Earth Sci., 49, 895–913, 2012.

568 Mottaghy, D. and Rath, V., Latent heat effects in subsurface heat transport modelling and their impact on
569 palaeotemperature reconstructions, Geophysical Journal International, 164, 236-245, 2006

570 Neukom, R., Gergis, J., Karoly, D.J., et al. Inter-hemispheric temperature variability over the past
571 millennium, Nature Climate Change, 4, 362–367, 2014.

572 Nicolussi, K. and Patzelt, G., Discovery of early Holocene wood and peat on the forefield of the Pasterze
573 Glacier, Eastern Alps, Austria, The Holocene, 10, 191–199, 2000.

574 Rath, V. and Mottaghy, D., Smooth inversion for ground surface temperature histories: estimating the
575 optimum regularization parameter by generalised cross-validation, Geophysical Journal International, 171
576 (3), 1440-1448, 2007

577 Rath, V., Gonzalez-Rouco, J. F. and Goosse, H., Impact of postglacial warming on borehole reconstructions
578 of last millennium temperatures, Climate of the Past, 8, 1059-1066, 2012.

579 Rodder, T. and Kneisel, C., Influence of snow cover and grain size on the ground thermal regime in the
580 discontinuous permafrost zone, Swiss Alps. Geomorphology, 175-176, 176–189, 2012.

581 Safanda, J. and Rajver, D., Signature of the last ice age in the present subsurface temperatures in the Czech
582 Republic and Slovenia, Global and Planetary Change, 29, 241-257, 2001.

583 Schmid, M.O., Gubler, S., Fiddes, J. and Gruber, S., Inferring snowpack ripening and melt-out from
584 distributed measurements of near-surface ground temperatures, The Cryosphere, 6, 1127–1139, 2012.

585 Schmidt, S., Weber, B. and Winiger M., Analyses of seasonal snow disappearance in an alpine valley from
586 micro- to meso-scale (Loetschental, Switzerland), Hydrol. Process., 23, 1041–1051, 2009.

587 Serra-Capizzano, S., A note on the antireflective boundary conditions and fast deblurring models, SIAM
588 Journal on Scientific Computing, 25-4, 1307–1325, 2004.

589 Shen, P. Y., Wang, K. H. and Beltrami Mareschal, J.C., A comparative study of inverse methods for
590 estimating climatic history from borehole temperature data, Palaeogeogr.Palaeoclimatol. Palaeoecol. (GPC
591 section), 98, 113-127, 1992.

592 Trachsel, M., Grosjean, M., Larocque-Tobler, I., Schwikowski, M., Blass, A., Sturm, M., Quantitative summer
593 temperature reconstruction derived from a combined biogenic Si and chironomid record from varved
594 sediments of Lake Silvaplana (south-eastern Swiss Alps) back to AD 1177. Quaternary Science Reviews, 29,
595 2719-2730, 2010.

596 Trachsel, M., Kamenik, C., Grosjean, M., McCarroll, D., Moberg, A., Brázdil, R., Büntgen, U., Dobrovolný,
597 P., Esper, J., Frank, D. C., Friedrich, M., Glaser, R., Larocque-Tobler, I., Nicolussi, K. and Riemann D.,
598 Multi-archive summer temperature reconstruction for the European Alps, AD 1053–1996, Quaternary
599 Science Reviews, 46, 66-79, 2012.

600 Zhang, T., Influence of the seasonal snow cover on the ground thermal regime: An overview, Rev. Geophys.,
601 43, RG4002, 2005.

602 Zhang, T. and Stamnes K., Impact of climatic factors on the active layer and permafrost at Barrow, Alaska,
603 Permafrost Periglacial Processes, 9, 229–246,1998.

604

7 ACKNOWLEDGEMENTS

612

Figure and Table Captions

614 Figure 1. Study area: (a) Location of the study area with the surrounding glaciers and the reconstructed
615 glaciers limits of the area (VPG = Vedretta Piana Glacier; TFG = Trafoi Glacier; SG = Solda Glacier; LMG = La
616 Mare Glacier; PACE = Pace Borehole; SSB = Share Stelvio Borehole; (b) View of the drilling equipment during
617 the realization of the SSB borehole in summer 2009.

618 Figure 2. Topography of the SSB site: a) Digital Elevation Model (5 m resolution) of the SSB site and b) SSW-
619 NNE (solid line) and N-S (dashed line) transects through the Stelvio summit. Horizontal and vertical scales
620 as well as thermistor chain position and depths are plotted to the same scale.

621 Figure 3. Example of a GST history parametrized by equation (2).

622 Figure 4. Synthetic data for the present time. It is remarkable that also varying the alpha value by 33% the
623 reconstructed GST does not vary significantly. Legend: 0.1 = blue line; 0.15 = green line; 0.2 = orange line.

624 Figure 5. Synthetic data for three past years (2013, 2014 and 2015). It can be seen that the inversion in the
625 last 50 years is more accurate than the inversion of Fig 4. Legend: 0.15 = green line; 0.2 = orange line; 0.25 =
626 red line.

627 Figure 6. Share Stelvio Borehole (SSB) Stratigraphy. Legend: (A) facies a (massive dolostone from grey to
628 pinky grey); (B) facies b (white dolostone); (C) facies c (black stratified limestone); (D) facies d (light brown
629 dolostone).

630 Figure 7. SSB mean annual ground temperature profiles on 2013, 2014 and 2015.

631 Figure 8 Effects of different thermal diffusivity used in the model. The temperature profiles *a posteriori* of
632 2015 obtained in the case of a constant thermal diffusivity value of the more widespread facies (a) (red
633 dots) and in the case of with a multilayers thermal diffusivities according the different facies according Fig.
634 6 (blue dots). The bars indicate the variations of the measured temperature in the same year.

635 Figure 9 Example of different GST history with different alpha with the extreme of heat flow values known
636 for the region. Legend: green lines are obtained with a heat flow of 70 mWm^{-2} while red lines with 85

mWm^{-2} . The different symbols indicate different alpha value (0.95 = solid line; 1.1 = empty dots; 0.8 = triangles).

Figure 10. Comparison between the anomaly of the mean annual GST reconstructed by SSB borehole (black thick line), its uncertainty range (red shaded) and MAAT anomaly reconstructed for the European Alps by Christiansen and Ljungqvist (2011) (grey line with dots; data available online at: ttps://www.ncdc.noaa.gov/paleo/study/12355) both respect the same reference period (1880-1960).

Figure 11. Trend of monthly mean of GST (red line) and Air temperature (blue line) at SSB since 1998. The red and blue dashes lines are respectively the linear regression of the GST and Air temperature.

Figure 12. Effect of the snow cover at SSB. The winter 2010/11 is representative of the average conditions of the snow cover at SSB while the following season 2011/12 was the snowiest of the whole monitoring period. The difference between the daily mean GST and air temperature (ΔGSTair; black line) shows the greater values during the greater drop of the air temperature (green line) during the winter due to the insulating effect of the snow cover (blue line) whereas the few episodes of high ΔGSTair in the summer are may due to the solar radiation that warms up the ground surface.

Figure 13. Main climatic events enhanced by anomalies of MAAT through different proxy in all Europe: A, (modified from Luterbacher et al., 2004); Central Europe: B, (rielaborated from Dobrovolný et al., 2010; Alps: C, (modified from the same data of Figure 5, Christiansen and Ljungqvist, 2011) and SSB: D, (this paper).

Figure 14. Comparison of predictions of the forward model for the same GST and different geometrical setups. Legend: 1D = red dots; 2D flat terrain = blue line; 2D N-S green line; 2D SSW-NNE orange line; 3D dashed black line. (See the Appendix for the details).

Table 1. Thermal gradients (°Cm-1) on 2013; 2014 and 2015 in the different depth intervals of the profile below the zero-annual amplitude that is approximately at 20 m of depth.

Table 2. Thermal properties of the three different facies occurred in SSB borehole measured in the Laboratory at three different steps of temperature (0; -1 and -2°C).

Table 1

	20-60 m (°Cm^{-1})	60-105 m (°Cm^{-1})	105-125 m (°Cm^{-1})	125-205 m (°Cm^{-1})	205-215 m (°Cm^{-1})	215-235 m (°Cm^{-1})	60-235 m (°Cm^{-1})
2013	0.0088	-0.0072	-0.0048	-0.0075	-0.0128	-0.0058	-0.0072
2014			-0.0046	-0.0074	-0.0128	-0.0056	
2015	0.0086	-0.0077	-0.0045	-0.0073	-0.0128	-0.0055	-0.0072

669   Table 2

	Density (gcm^{-3})	Diffusivity (10^{-6}m^{2}s^{-1})	Heat capacity (Jg^{-1}K^{-1})	Conductivity (Wm^{-1}K^{-1})
Facies a	2.7			
0°C		2.2	0.7	4.5
-1°C		2.1	0.8	4.4
-3°C		2.1	0.8	4.4
Facies b	2.8			
0°C		2.8	0.8	6.2
-1°C		2.8	0.8	6.2
-3°C		2.8	0.8	6.2
Facies c	2.7			
0°C		2.0	0.8	4.0
-1°C		1.9	0.8	3.9
-3°C		1.9	0.8	4.0

670

Appendix 1: Details of the regularization and inversion technique

672   The temperature anomaly in the borehole at time t at depth z is modeled by the solution of the heat
673   equation

$$\frac{\partial A}{\partial t} - \frac{\partial}{\partial z}\left(\kappa \frac{\partial A}{\partial z}\right) = 0 \quad (1)$$

674   for the domain $(t, z) \in (-t_{max}, 0) \times (0, z_{max})$. If the boundary data A(t,0) is piece-wise constant, then
675   the solution of the direct problem for equation (1) can be found explicitly (see Carlsaw and Jaeger, 1959). In
676   fact, the anomaly observed in the borehole t years ago, originating from a GST that has been constant
677   except for an increase of δ °C between t_2 and t_1 years ago is:

$$A(t, z) = \delta \left[erfc\left(\frac{z}{\sqrt{4\kappa(t_2 - t)}}\right) - erfc\left(\frac{z}{\sqrt{4\kappa(t_1 - t)}}\right) \right]$$

678   The above formula of course makes sense only for $t < t_1$ and the value $t = 0$ corresponds to present time.
679   For the purpose of reconstructing the GST history, it is customary to approximate it with a piece-wise
680   constant function (see Figure 3)

$$GST(t) = \begin{cases} \tau_k, & t \in [-t_k, -t_{k-1}] \\ \tau_\infty, & t \leftarrow t_N \end{cases} \quad (2)$$

681   where t_k, for k = 1,…,N, is the sequence of times in the past where we want to compute the value of the
682   GST, and the τ_k's are the unknown values to be computed. The prediction of model (1) for the borehole
683   temperature t years ago, originating from the GST (2) is

$$A(z, t) = \tau_1 \varphi(z, t_1 - t) + \sum_{k=1}^{N} \tau_k [\varphi(z, t_{k+1} - t) - \varphi(z, t_k - t)] - \tau_\infty \varphi(z, t_N - t), \quad (3)$$

684 where $\varphi(z,t) = erfc\left(\frac{z}{\sqrt{4\kappa t}}\right)$. Note that, once the sequence t_k is chosen, the relation between the borehole

685 temperature at depth z_j predicted by the model and the unknown values τ_k of the GST anomaly is thus

686 linear. The matrix L of the linear system (4) in the main text is thus

$$L_{j,1} = \varphi(Z_j, t_1 - T_j)$$
$$L_{j,k} = \varphi(Z_j, t_{k+1} - T_j) - \varphi(Z_j, t_k - T_j)$$
$$L_{j,N+1} = \varphi(Z_j, t_N - T_j).$$

687 We point out that each row of the matrix L can have a different value of T_j, so that the GST reconstruction

688 can be based not only on a single temperature profile, but also on the variation of the temperature profile

689 between the present and some years ago. Further, it is not needed that the reconstruction times t_k are

690 equally spaced in the past.

691 Given the detrended measures $\vec{m}$, we must compute the vector $\vec{\tau}$ solving the linear system (4). Note that

692 the inverse problem for the heat equation (1) is well-known to be severely ill-posed, the matrix L is strongly

693 ill-conditioned and its singular values decay exponentially to zero, with related singular vectors largely

694 intersecting the subspace of high frequencies (Serra-Capizzano, 2004). Therefore, since the right-hand side

695 $\vec{m}$ is affected by error measurements, solving directly the linear system (4) would lead to a computed GST

696 that would be highly oscillating and very far from the true physical values for $\vec{\tau}$. It is then necessary to

697 introduce a regularization process by modifying the original problem (4), in order to obtain an

698 approximation that is well posed and less sensitive to errors in the right-hand-side of (4). The Tikhonov

699 regularization usually provides better restorations than the trucated SVD, because it is characterized by a

700 smooth transition in the filtering of the frequencies and the smoothness of the transition can be somehow

701 chosen by manipulating the regularization parameter of the method (Hansen, 1998). In this paper, we thus

702 propose the use of the generalized Tikhonov regularization, where the damping term is measured by a

703 proper seminorm. In practice, instead of dealing with the linear system (4), we solve the minimization

704 problem

$$\min_{\vec{\tau}}\|L\vec{\tau} - \vec{m}\| + \alpha\|R\vec{\tau}\| \quad (5)$$

705 where $\alpha > 0$ is the regularization parameter and R is the regularization matrix. The presence of the matrix

706 R in (5) allows to impose some a-priori information on the true solution. Indeed, when minimizing (5), the

707 components of the solution belonging to $ker(R) = \{\vec{x}\, s.t.\, R\vec{x} = \vec{0}\}$ are perfectly reconstructed. In fact, if a

708 vector x belongs to ker(R) then ||Rx||=0 and hence the penalization term disappears in the minimization

709 problem (5) and consequently the data are perfectly fitted. Note that in order to guarantee the uniqueness

710 of the solution (5), the condition $ker(L) \cap ker(R) = \vec{0}$ has to hold.

711 In this paper, we use as regularizer a standard discretization of the Laplacian

712

$$R = \begin{pmatrix} -1 & & & & & \\ 2 & & & & & \\ -1 & & -1 & 2 & -1 & & \ddots & \ddots \\ \ddots & -1 & 2 & -1 & & \\ & & -1 & & & \end{pmatrix}$$

713 of size $(N - 2) \times N$ and hence the constant and linear components of the solution are not damped in the
714 Tikhonov regularization (5).

715

Appendix 2: comparison of 1D and higher dimensional models for SSB

717 In order to ascertain the effect of the terrain geometry we conducted a number of forward simulations
718 with the model (1) using as boundary data the synthetic GST shown in Fig 4 (dashed line) and already
719 employed for the sensitivity analysis.

720 First we computed the solution of the one-dimensional model (1). Next we computed the solution of the
721 corresponding three-dimensional model in a computational domain of 400X400 m centred around SBB and
722 500 m deep, whose the top surface was obtained from a DEM (with a resolution of 10m . Such domain was
723 discretized with the GMSH program and the heat equation was solved using linear Lagrange finite elements
724 in space and backward Euler in time. The mesh was refined until numerical convergence was observed and
725 in Figure 14 we present the results for a mesh with 1.3 million of tetrehedra. The numerical simulations
726 were performed with the HPC cluster of the Dipartimento di Matematica of the Università di Torino.

727 Figure 14 compares the temperature anomalies that each of the models would predict at SSB at present
728 time. The red dots are the predicted well anomalies at the depth of the thermometers at SSB. One can see
729 that the predictions of the two-dimensional model with flat terrain (blue line) almost coincide with those of
730 the one-dimensional one. Furthermore, the two-dimensional model applied to the section with the steeper
731 sides (the SSW-NNE one, orange line) gives rise to predictions that are within the instrumental error
732 (±0.1°C) whereas the N-S section (red line), which has a flatter terrain, gives rise to predictions that are
733 quite close to those of the one-dimensional model. The predictions of the 3D model (dashed black line) are
734 very close to the 2D flat and the 2D N-S (with difference always < 0.03°C).

735 Finally, let us remark that for the forward model, a numerical 3D simulation takes hours to complete on 16
736 computing nodes of our HPC cluster. Using a numerical multi-dimensional simulator in the inverse problem
737 would of course require to compute several times the forward model and would thus take a lot longer than
738 the few seconds in which our proposed method can compute the reconstructed GST depicted in Fig. 10.

739

740

741

742

743

744

745

746

747

748

749

750

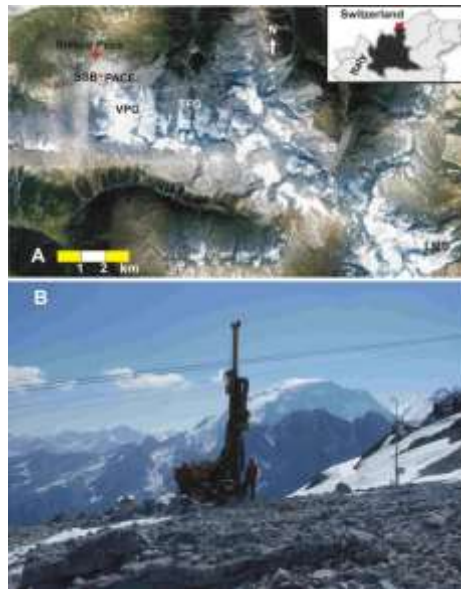751   Fig. 1

752

753

754

755

756

757

758

759

760

761

762

763

764
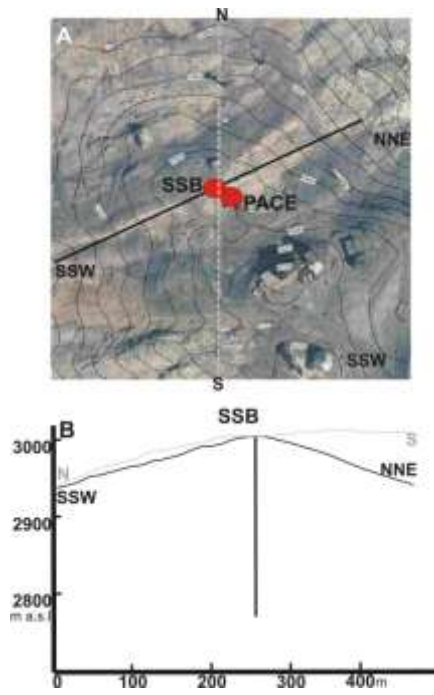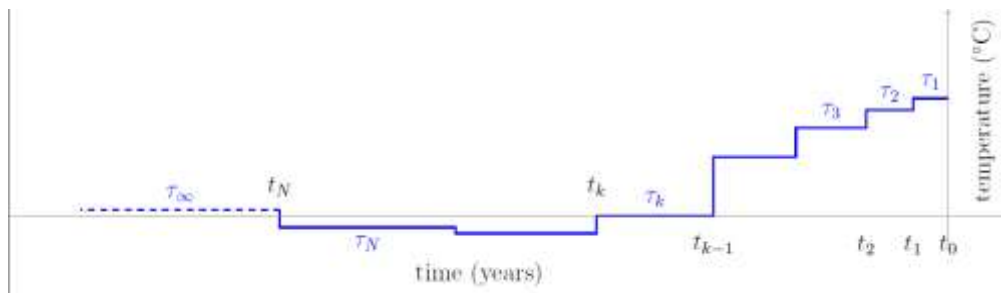
765   Fig. 2
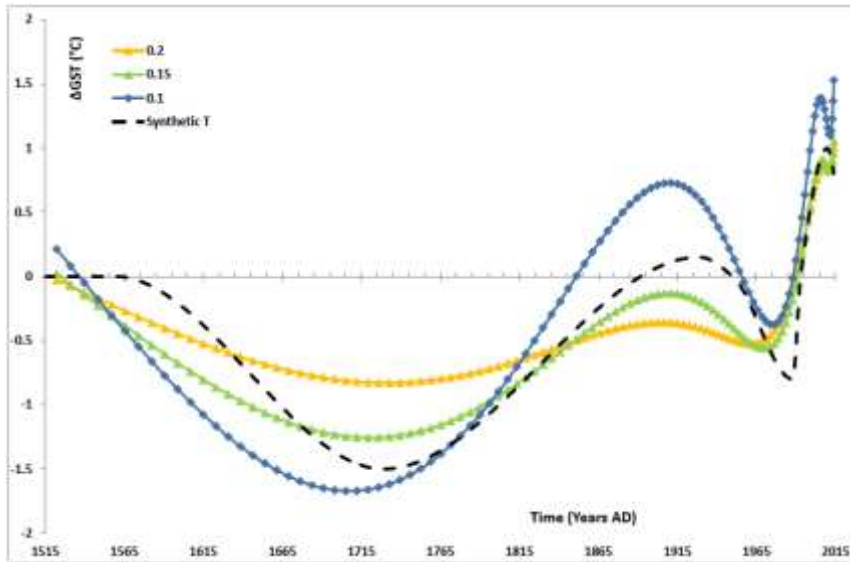
766

767

768

769   Fig.3

770

771

772

773

774

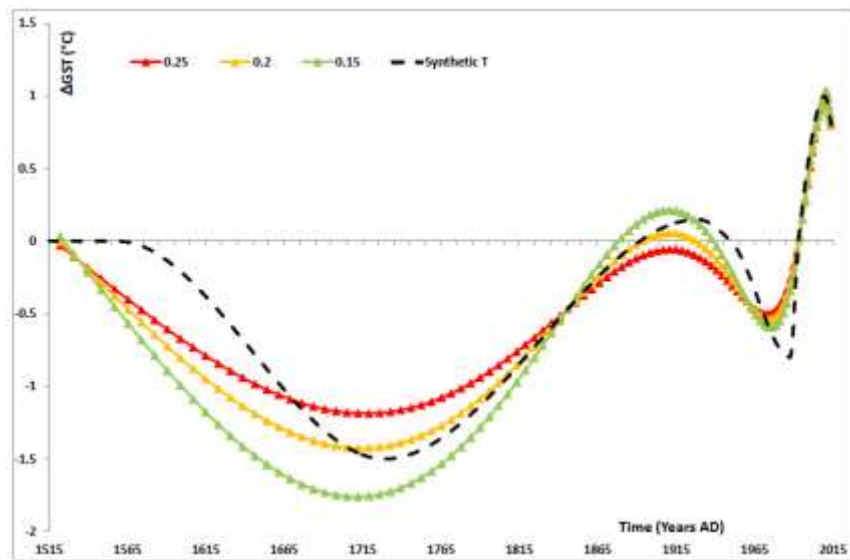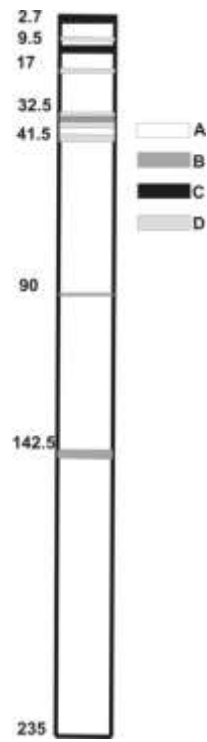775

776

777

778

779

780   Fig.4
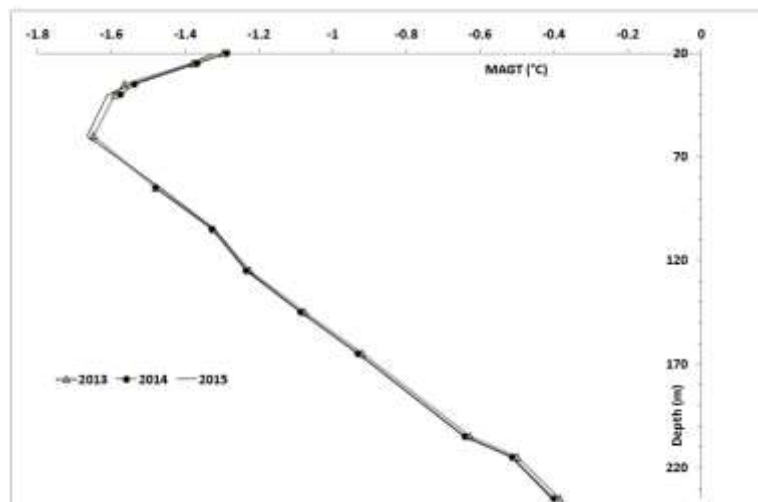
781

782

783   Fig. 5

784

785

786

787

788

789

790

791

792

793

794

Fig. 6

795

796

Fig. 7

797

798

799

800

801

802

803

804

805   Fig. 8

806
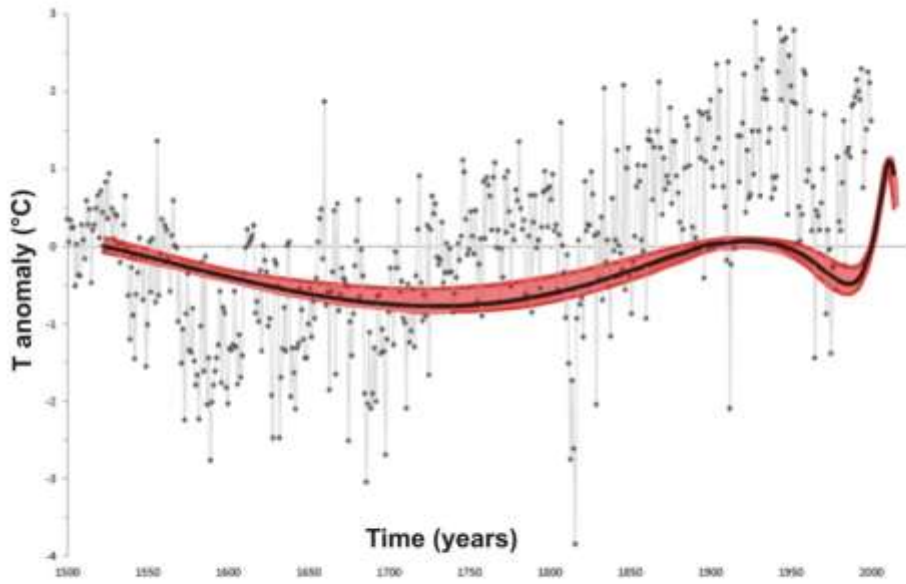
807

808   Fig. 9
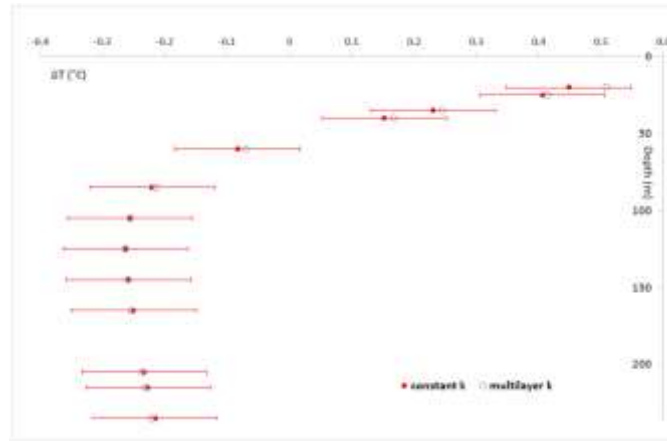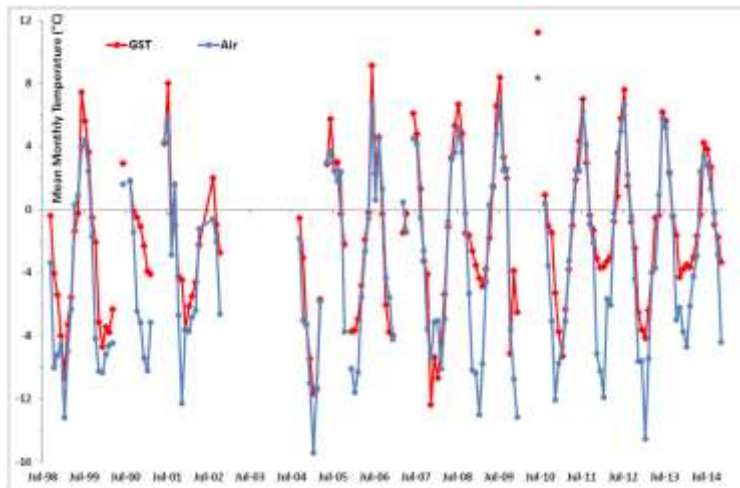
809
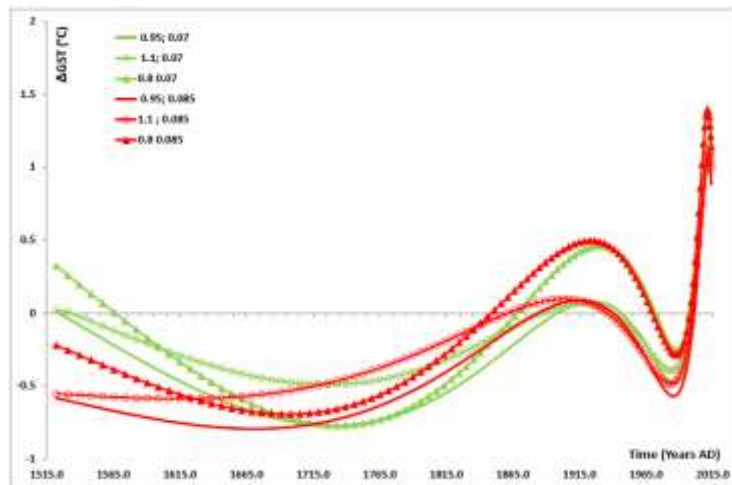
810

811

812

813

814

815

816

817

818

819   Fig. 10

820

821

822

823

824
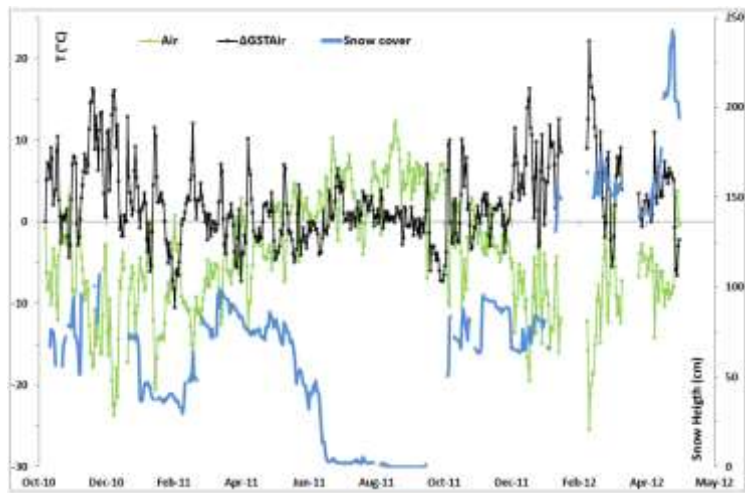
825   Fig. 11

826

827

828

829   Fig. 12

830

831
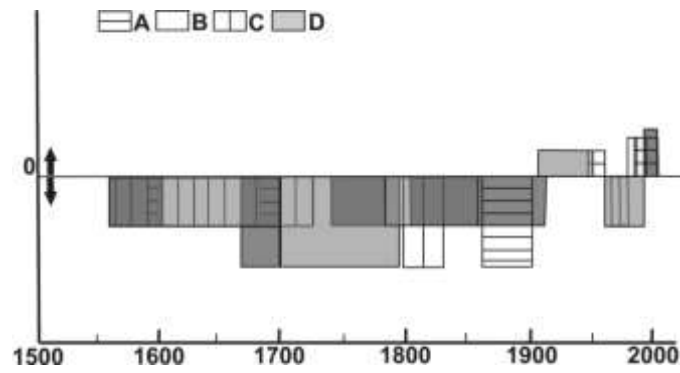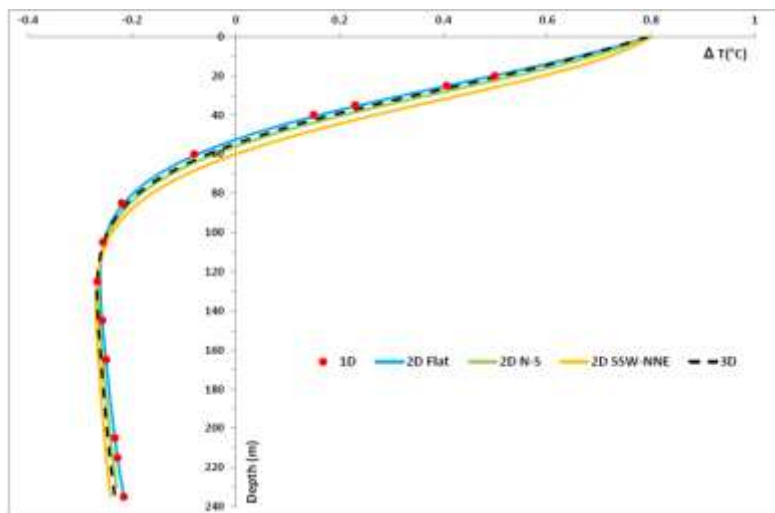
832   Fig. 13

833

834   Fig. 14

835

836